Magnetic Resonance in Medicine 64:787–798 (2010)

Simultaneous Myocardial Strain and Dark-Blood Perfusion Imaging Using a Displacement-Encoded MRI Pulse Sequence

Yuan Le,[1] Ashley Stein,[1] Colin Berry,[2] Peter Kellman,[1] Eric E. Bennett,[1] Joni Taylor,[1] Katherine Lucas,[1] Rael Kopace,[1] Christophe Chefd'Hotel,[3] Christine H. Lorenz,[3] Pierre Croisille,[4] and Han Wen[1]*

The purpose of this study is to develop and evaluate a displacement-encoded pulse sequence for simultaneous perfusion and strain imaging. Displacement-encoded images in two to three myocardial slices were repeatedly acquired using a single-shot pulse sequence for 3 to 4 min, which covers a bolus infusion of Gadolinium contrast. The magnitudes of the images were T_1 weighted and provided quantitative measures of perfusion, while the phase maps yielded strain measurements. In an acute coronary occlusion swine protocol (n = 9), segmental perfusion measurements were validated against microsphere reference standard with a linear regression (slope 0.986, R^2 = 0.765, Bland-Altman standard deviation = 0.15 mL/min/g). In a group of ST-elevation myocardial infarction patients (n = 11), the scan success rate was 76%. Short-term contrast washout rate and perfusion are highly correlated (R^2 = 0.72), and the pixelwise relationship between circumferential strain and perfusion was better described with a sigmoidal Hill curve than linear functions. This study demonstrates the feasibility of measuring strain and perfusion from a single set of images. Magn Reson Med 64:787–798, 2010.

Key words: ischemia; viability; myocardial perfusion; strain; first pass; DENSE

Regional contractile function and perfusion are two key indices in the diagnosis and prognosis of ischemic heart disease. MRI can accurately assess myocardial wall motion and strain through several techniques, including tagged MRI (1–4), velocity-encoded MRI (5), and displacement-encoded MRI (6–8). Contrast-enhanced imaging, including first-pass (9–15) and delayed hyperenhancement MRI (16–21), provides information on the perfusion and viability status of the myocardial tissue. Whether the clinical situation is to assess the efficacy of reperfusion strategy with greater accuracy or to recognize patients who would require further therapy, the knowledge of both regional myocardial function and perfusion is helpful in differentiating among the various scenarios.

[1]National Heart, Lung, and Blood Institute, National Institutes of Health, Bethesda, Maryland, USA.

[2]Western Infirmary & Associated Hospital, Department of Cardiology, Glasgow, Scotland.

[3]Siemens Corporate Research, Inc., Princeton, New Jersey, USA.

[4]Departement de Radiologie, Hôpital Cardiologique et Pneumologique, L. Pradel, Lyon, France.

*Correspondence to: Han Wen, Ph.D., National Institutes of Health, Bldg 10, B1D416, 10 Center Dr., Bethesda, MD 20892. E-mail: wenh@nhlbi.nih.gov

Received 27 October 2009; revised 19 February 2010; accepted 1 March 2010.

DOI 10.1002/mrm.22461
Published online 11 June 2010 in Wiley Online Library (wileyonlinelibrary.com).

An MRI pulse sequence capable of measuring myocardial perfusion and strain in a single data set, which thus far has not been generally possible in humans, would save scan time and facilitate perfusion-function correlation by eliminating the problem of registration. Imaging techniques that combine myocardial strain and delayed hyperenhancement imaging have been reported by several groups (22,23). However, these techniques employed interleaved acquisition of multiple images, which are combined into single-strain and delayed hyperenhancement images; therefore, they are not suited for first-pass perfusion imaging due to the time constraints.

The purpose of this study is to develop a pulse sequence for simultaneous perfusion and strain imaging, to validate the perfusion measurement in a swine model, and to assess its performance in a group of acute myocardial infarction patients.

The pulse sequence is a single-shot, multislice displacement-encoded (DENSE) (7) sequence. It was used to collect displacement-encoded images in every other heartbeat over several minutes, covering the first-pass and initial washout of the contrast agent (24,25). An arterial input function (AIF) slice was acquired concurrently. This approach differs from current saturation-recovery perfusion sequences in that the DENSE images are positively T_1 weighted, meaning that the signal intensity decreases with shortened T_1. As a result, the myocardial tissue that receives the contrast agent becomes dark, while the ischemic segments remain bright. Additionally, the ventricular cavities are dark due to rapid blood flow and high contrast-agent concentration (7).

MATERIALS AND METHODS

Animal Protocol

The protocol was approved by the NIH Animal Care and Use Committee. Yorkshire farm pigs (n = 9, weight 28-86 kg, all males) were maintained under anesthesia with isoflurane (2-3%) and monitored by their heart rate, blood pressure, and pCO_2 level during the entire experiment. In six pigs, left-side thoracotomy exposed either the left anterior descending (LAD) or left circumflex (LCX) arteries, and these were ligated to effect total occlusion. One coauthor is an interventional cardiologist and was available to perform percutaneous LAD occlusion with balloon occluders in the other three pigs. MRI was performed immediately after the occlusion, followed by the injection of fluorescent microspheres (NuFlow®,

IMT Laboratories, Irvine, CA; or FluoSpheres®, Invitrogen, Carlsbad, CA) into the left atrium. Concurrent arterial blood samples were taken from the femoral artery for calibration of the microsphere counts. The animal was then euthanized and the heart was excised and embedded in agarose gel. The gelled samples were oriented in accordance with the MRI short-axis scan planes in vivo, using a two-axis gimbal mount (26). Five of the nine hearts were sliced into 4-5mm slices, sectioned into tissue samples according to the American Heart Association segmentation scheme (27), and sent to IMT for flow measurement. The other four hearts were sent to Barlow Scientific (Olympia, WA) for three-dimensional microsphere imaging and flow measurement.

Patients

Between April, 2, 2008, and July, 18, 2008, 13 patients who presented with first acute ST-elevation myocardial infarction (STEMI) (11 men, two women, age range 39-82 years) were recruited as part of a Health Insurance Portability and Accountability Act–compliant institutional review board–approved protocol. Inclusion criteria were presence of a complete occlusion (Thrombolysis in Myocardial Infarction (TIMI) score 0) of a single culprit coronary artery, successful angioplasty with a patent infarct-related artery with a final TIMI score of 3 (within 6 hours of symptom onset), and presence of no-reflow segments in the myocardial wall, based on delayed hyperenhancement images. MRI was performed at 2 days after angioplasty. Informed consent was given by all patients. The data from two patients were excluded due to failure of electrocardiogram (ECG) triggering (a 52-year-old male) and misplacement of the AIF slice (a 67-year-old female), respectively (Fig. 1). In our institution, the cardiac patients who were most available for this study were STEMI postangioplasty patients who were stable enough to allow an MRI evaluation of the reperfusion treatment. In these patients, cardiac MRI examination provided comprehensive and high-quality prognostic information.

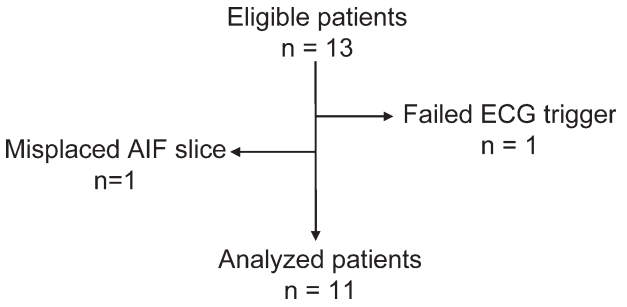

FIG. 1. Patient flow chart.

MRI Protocol

All MR scans were performed on a clinical 1.5-T scanner (Siemens Magnetom; Avanto, Erlangen, Germany). Three to four short-axis slices were acquired in every other heartbeat and repeated 90 times (three encoding directions × 30 repetitions) over a period of 3 to 4 min or 180 heartbeats. The imaging sequence (Fig. 2) was a multislice single-shot DENSE sequence (7) with true Fast Imaging Steady-state Precession (FISP) readout (6,28,29) detailed below.

The three displacement-encoding gradients were combinations of in-plane and through-slice moments of Y + Z, −Y + Z and X + Z respectively, where X, Y, and Z are the readout, phase-encode, and through-slice directions (28). The same through-slice encoding moment was applied to all three images, while the in-plane encoding gradients varied among them. The uniform through-slice encoding served to suppress the unwanted T_1 recovery and conjugate echoes in all three images. In postprocessing, the three phase maps were linearly recombined to produce X by 2(X + Z) − (Y + Z) − (−Y + Z) and Y by (Y + Z) − (−Y + Z) encoded phase maps and remove any phase errors from off-resonance, radiofrequency, and other systematic factors (28). The X- and Y-encoding moments were 0.38 rad/mm in pigs and 0.27 rad/mm in patients. The Z-encoding moment was 4.8 rad per slice thickness. This value was found to be sufficient to suppress the free induction decay and conjugate echo signals (8,30). Additionally, the uniform through-slice encoding moment meant that the image intensity would not be affected by the encoding directions and only varied with the influx of the contrast agent.

Other imaging parameters included tFISP echo spacing of 2.5 ms, matrix size of 128 × 40 with inner-volume excitation equivalent to 128 × 96 and 3/4 phase-encode field of view, in-plane resolution of 2.5mm in pigs and 3.5mm in patients, and slice thickness of 6-8mm. Ramped-flip-angle (30°-75°) readout (6) was also implemented to equalize the echo train amplitude.

Figure 2 shows the events in a heartbeat: the displacement-encoding segment was placed immediately after the QRS trigger, followed by the acquisition of the saturation-recovery arterial-input-function image, and then sequential acquisitions of the two to three displacement-encoded slices. The AIF slice was positioned at the left ventricular (LV) base and acquired with fast gradient-recalled-echo readout of echo time of 1.2 ms, without refocusing the displacement-encoding moments. The DENSE slices were positioned to cover the territory of the occluded artery. At the end of an examination, a proton-density image of the AIF slice was also acquired for the purpose of calibration.

The saturation-recovery time of the AIF slice was 50 ms. The mixing time (Tm) (T_1 weighting) of the DENSE slices were from 200 ms for the first slice to 400 ms for the third slice. The acquisition time of each slice was 100 ms. In all, a data set contained 270-360 images of 3-4 (slices) × 3 (encoding directions) × 30 (repetitions). At 30 sec after the start of scan, Gd contrast was given intravenously at a dose of 0.1 mmol/kg and a rate of 2.0 mL/sec in the pigs and at a higher infusion rate of 4.0 mL/sec in patients. The different infusion rates were scaled according to the total amount of contrast. The swine study was carried out in the United States and used Gadolinium-diethylenetriamine pentaacetate (Gd-DTPA) (Magnevist; Bayer HealthCare Pharmaceuticals Inc.,

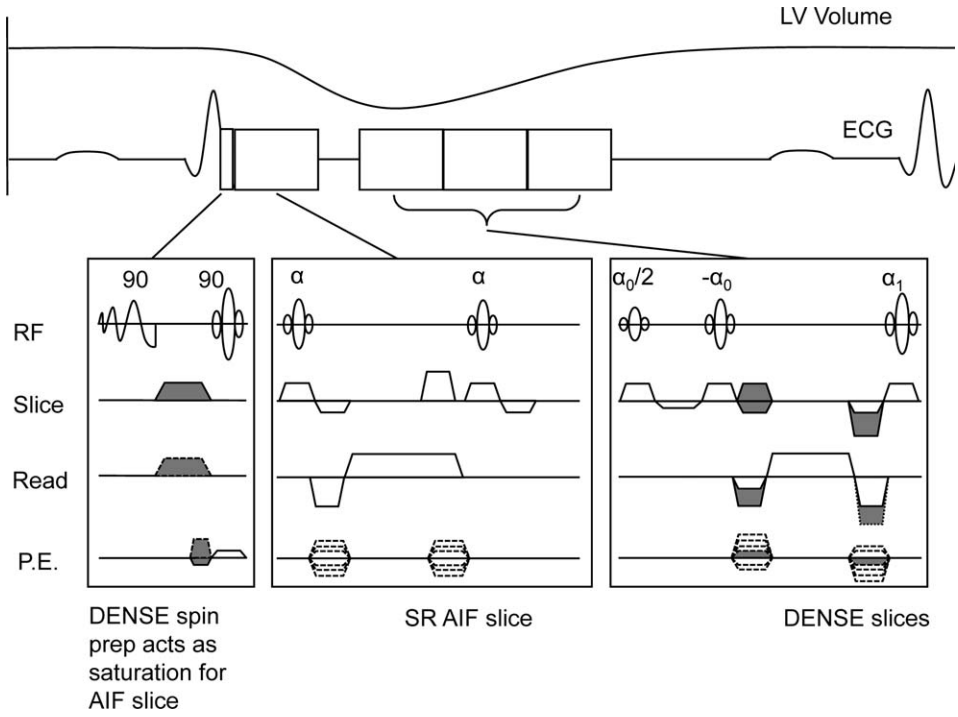

FIG. 2. Pulse sequence and ECG triggering scheme. The displacement-encoding section starts immediately after the QRS trigger. This is then followed by the single-shot acquisition of the arterial-input-function slice, using a fast gradient-recalled-echo readout. Starting at 150 ms after the encoding segment, the three DENSE slices are acquired sequentially, using a single-shot ramped-flip-angle true-FISP readout. Each slice takes 100 ms to acquire. At the very end of the examination, a proton-density reference for the AIF slice was acquired by turning off the displacement-encoding segment.

Wayne, NJ). The patient study was performed in Lyon, France, where gadolinium-tetraazacyclododecanetetraacetate (Gd-DOTA) was the standard contrast agent and used in the study.

Image Processing

All DENSE images were warp-registered to correct for respiratory motion (31–33). Perfusion and circumferential strain maps were obtained from the magnitude and phase of the DENSE images, respectively. Circumferential strain was calculated from each set of three encoding directions, using software running in Windows or MAC operating systems (DENSEView, National Institutes of Health, Bethesda, MD) (28). The 30 repetitions yielded 30 strain measurements, and the final strain map was the signal-to-noise ratio (SNR)-weighted average of the 30 measurements (34):

$$Ecc(x,y) = \frac{\sum_{n=1}^{30}\left[Ecc_n(x,y)I_n^2(x,y)\right]}{\sum_{n=1}^{30} I_n^2(x,y)},$$
$$I_n(x,y) \quad = I_{n,1}(x,y)I_{n,2}(x,y)I_{n,3}(x,y), \qquad (1)$$

where $Ecc(x,y)$ is final strain value at each location (x,y), $Ecc_n(x,y)$ is the strain calculated using the nth set of images, $I_{n,1}(x,y)$, $I_{n,2}(x,y)$, and $I_{n,3}(x,y)$ are the three images of different encoding directions in the nth image set.

AIF image intensity in the descending aorta or the LV cavity was used to derive the arterial contrast concentration (35,36). Time intensity data of the myocardial pixels were then converted to absolute perfusion F and short-term washout rate k through a Fermi function-based deconvolution using the Marquardt-Levenberg algorithm (10,15). This is detailed in Appendix A.

The effect of image noise on the perfusion accuracy was investigated with Monte Carlo simulations and is described in Appendix B. The results showed that at the current sampling rate of one image every 2 sec, noise levels below 15% of the precontrast intensity gave acceptable accuracy in perfusion estimates. This was used as the threshold to exclude highly noisy pixels. The method to estimate the noise level in each pixel is also detailed in Appendix B.

Perfusion Measurement Validation

DENSE myocardial strain measurements have been validated in other studies. DENSE strain maps acquired during breath holding have been validated in normal volunteers (37,38). In patients, detection of abnormal wall motion by breath-hold DENSE has been validated against two-dimensional echocardiography (28). Free-breathing data acquisition followed by warp image registration was validated in a normal volunteer study (33). Our swine study focused on the accuracy of the perfusion measurement against microsphere reference standards. The MRI perfusion maps were segmented according to American Heart Association recommendation (27), and then MRI

and microsphere segmental perfusion values were compared using linear regression and Bland-Altman analysis.

Success Rate and Image Quality in Patients

In each patient the DENSE slices were visually scored by one author as "0 = failure," "1 = good," and "2 = excellent," according to the following criteria: a slice containing signal dropouts in the myocardial wall or apparent errors in image registration due to through-slice motion or other reasons is a failure, a slice that has no signal dropouts or apparent image registration errors is considered good, and a slice that has high signal-to-noise ratio and none of the above errors is rated excellent. The average success rate in all patients and the average score of all successful slices were calculated. The reasons for failures were investigated.

Correlation of Short-Term Contrast Washout Rate and Systolic Strain With Perfusion

Since the strain, perfusion, and washout rate maps came from the same images, they were inherently perfectly matched. This allows pixel-by-pixel correlation of different measurements. Pixels in the LV myocardial wall of the successful slices in all patients were pooled for linear regression between perfusion and contrast washout rate.

Similarly, pixel values of circumferential strain and perfusion were correlated using linear regression. Here it became necessary to exclude the last one of the three DENSE slices. The reason is that the three slices were acquired at delays of 200 ms, 300 ms, and 400 ms after the R-wave trigger, which means that the last slice was outside the end-systole plateau and did not provide end-systolic strain. Strain values in the first two slices were plotted against both the absolute perfusion and the normalized perfusion defined in each patient as the ratio of absolute perfusion over the average of the remote normal area. Since a previous study showed that the relationship between strain and perfusion may be better described by sigmoidal curves (39), both linear and sigmoidal Hill curves were used to fit the strain-perfusion data.

Statistical Analysis

The statistical analysis was performed using Microsoft Excel (Microsoft Corporation) and JMP (SAS Institute Inc.). All numerical results below are presented as mean with 95% confidence interval unless specified otherwise. Quality of curve fittings was evaluated by their Pearson correlation coefficient (R^2) values. Significance of linear regression was assessed with the F test. Significance of difference between two measurements was assessed with Wilcoxon signed rank test without assuming normal distribution.

RESULTS

Signal Intensity Curve in DENSE Images

Figure 3 shows the image time-intensity curves in normal and ischemic myocardium in a DENSE slice, as well as the LV blood pool in the saturation-recovery AIF slice. It can be seen that the intensity of the ischemic segments decreased less than that of the normal segments upon contrast infusion, thereby appearing bright immediately after infusion. The perfusion, strain, and washout rate maps of a patient are shown in Fig. 4. The low perfusion areas apparently match the areas of low strain and low washout rate.

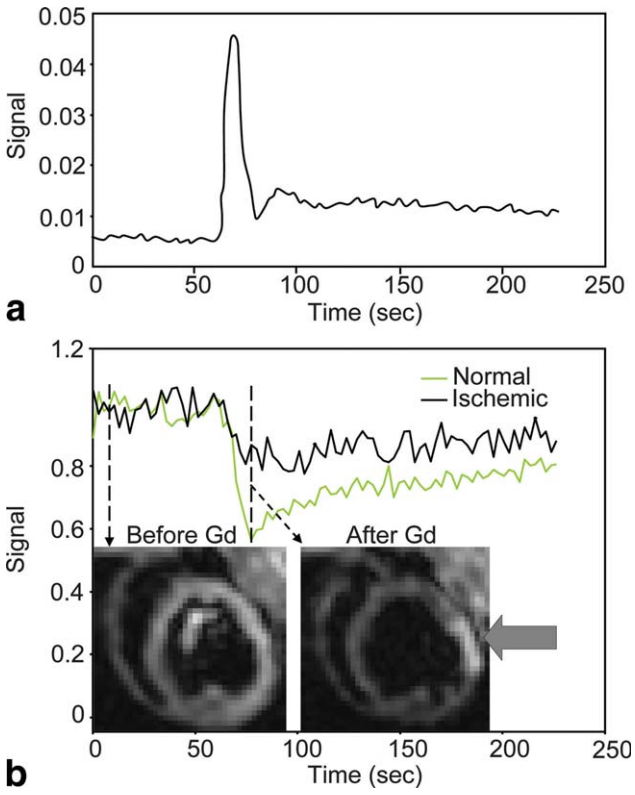

FIG. 3. Signal time-intensity curves in a pig heart. **a**: Intensity of the LV blood pool in the saturation-recovery AIF image. **b**: Intensity of the myocardium in a DENSE slice after Gd infusion. Arrow points to the ischemic segment. Due to the positive T_1 contrast of the image, normally perfused tissue became dark upon contrast arrival, while ischemic tissue retained its brightness. Ventricular cavities are dark due to rapid blood flow and high contrast concentration.

Perfusion Measurement Validation

MR perfusion maps and fluorescence microsphere images from a pig heart are shown in Fig. 5. It can be seen that areas of low fluorescence in Fig. 5c and d are matched with low MR perfusion in Fig. 5a and b. The regression between segmental MRI and microsphere perfusion values of all pigs is shown in Fig. 6. The correlation between the two is $R^2 = 0.765$ ($P < 0.01$). The slope is 0.986 (95% confidence interval = 0.88, 1.09). The intersection is 0.058 (95% confidence interval = −0.0047, 0.12), which is not significantly different from zero ($P = 0.07$).

Figure 7 shows the Bland-Altman plot for the same comparison. The standard deviation of the difference between the two measurements is ± 0.15 mL/min/g. The average of

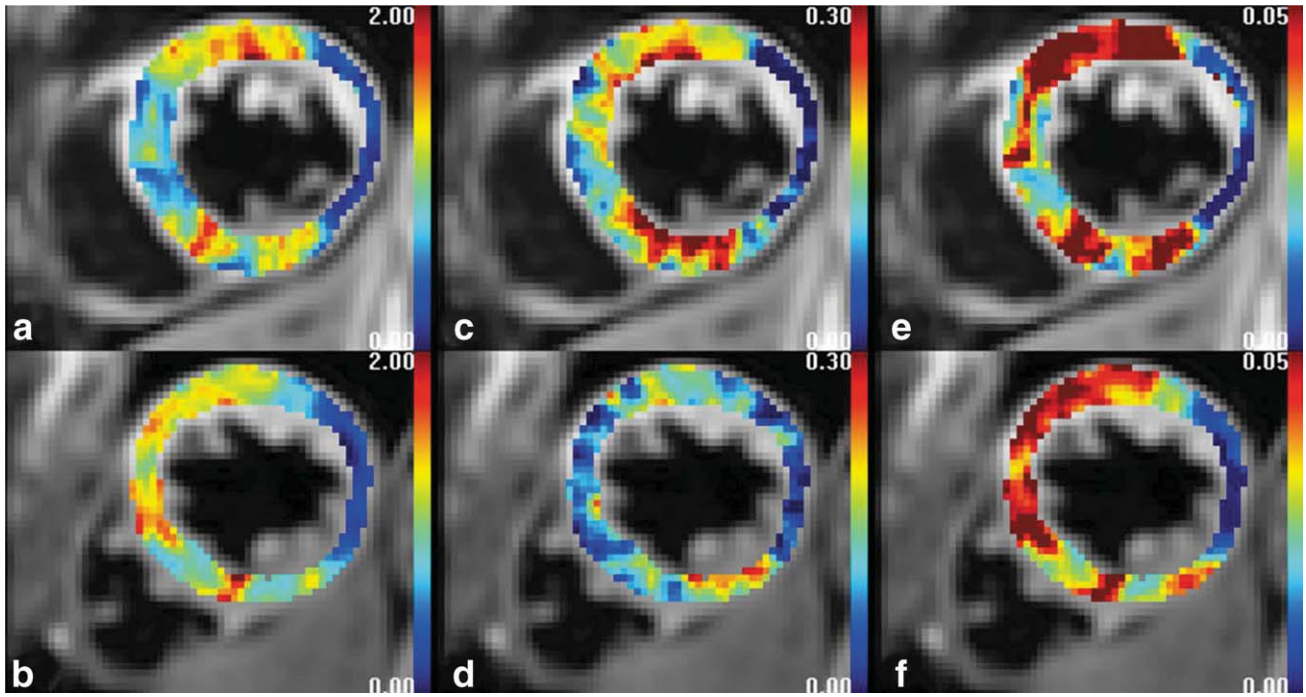

FIG. 4. The perfusion, strain, and short-term washout rate maps of a patient. **a,b**: The perfusion maps in units of ml/min/g. **c,d**: Corresponding circumferential strain maps. **e,f**: Corresponding short-term contrast washout rate maps in units of seconds.

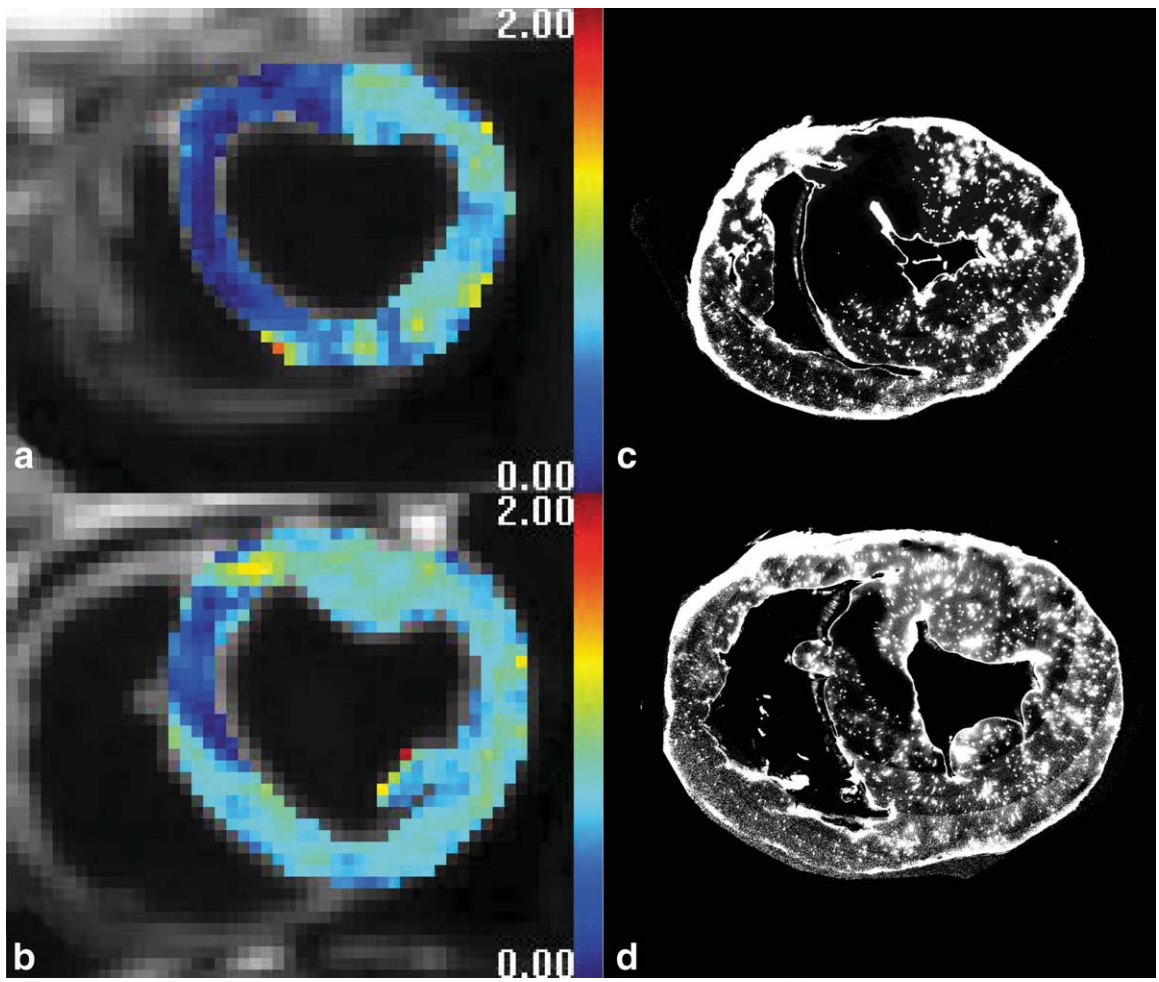

FIG. 5. **a,b**: MRI perfusion maps of the basal and midlevel slices of a pig heart in units of milliliters per minute per gram. **c,d**: Epifluorescence images of the microsphere distribution in the same slices.

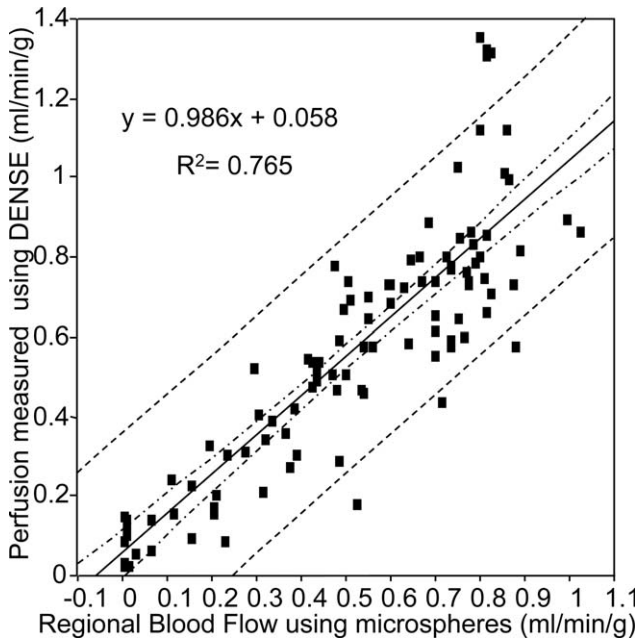

FIG. 6. Segment-by-segment regression of perfusion measured by DENSE versus regional blood flow by microspheres for all pigs. The dashed lines show the 95% prediction limit, the dot-dashed lines show the 95% confidence limit of the regression.

the difference is 0.05 mL/min/g, which is statistically not significant by Wilcoxon signed rank test ($P = 0.19$). The overall range of perfusion was from 0 to 1.2 mL/min/g.

Success Rate and Image Quality Assessment in Patients

Among all 33 DENSE slices of the 11 patients, eight slices were deemed failures. These included one due to signal dropouts and seven due to errors in image registration. The success rate was 76%, and the average score in successful slices was 1.44, or midway between good and excellent.

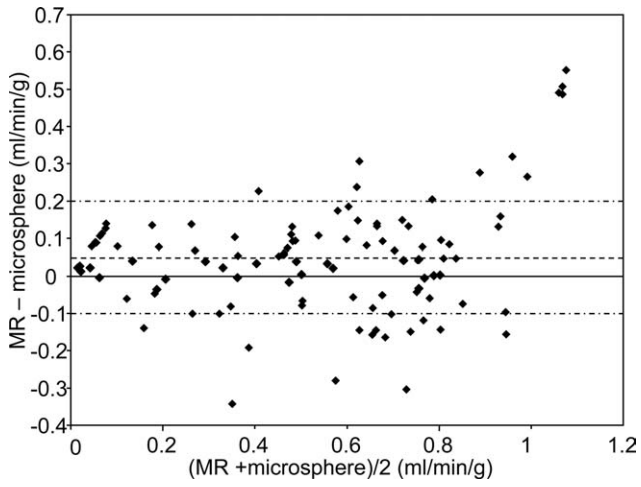

FIG. 7. Bland-Altman plot of perfusion measurement comparison of MR and microspheres. The mean difference (dashed line) was 0.05 mL/min/g. The standard deviation of the difference is ±0.15 mL/min/g.

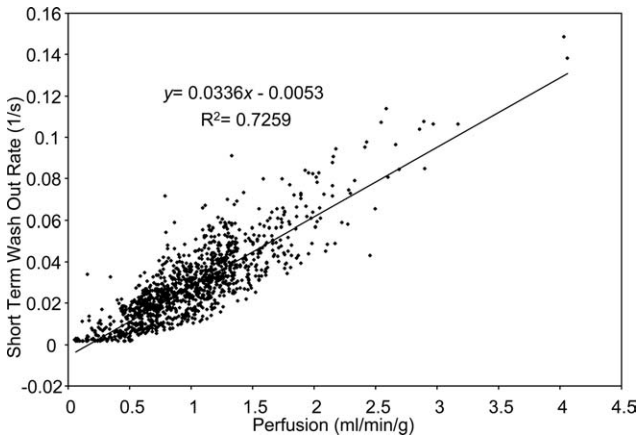

FIG. 8. Correlation of short-term washout rate versus perfusion in STEMI patients.

Correlation of Short-Term Contrast Washout Rate and Systolic Strain With Perfusion

Figure 8 shows that the short-term contrast washout rate was strongly correlated with absolute perfusion in patients with $R^2 = 0.726$ ($P < 0.01$). The slope of linear regression was 0.0336 (95% confidence interval = 0.0324, 0.0348).

Figure 9 shows the strain versus absolute perfusion data and curve fittings. The sigmoidal Hill fitting yielded a higher correlation ($R^2 = 0.211$) than linear regression ($R^2 = 0.164$, $P < 0.01$). Strain was better correlated with normalized perfusion than absolute perfusion in both linear regression ($R^2 = 0.288$, $P < 0.01$) and sigmoidal fitting ($R^2 = 0.308$) (Fig. 10).

The perfusion and circumferential strain from the pig study yielded somewhat higher correlation, with $R^2 = 0.496$. The normalized perfusion and circumferential strain had a correlation coefficient $R^2 = 0.493$.

DISCUSSION AND CONCLUSIONS

In this study, we developed a modified displacement-encoded MRI sequence and demonstrated its ability to

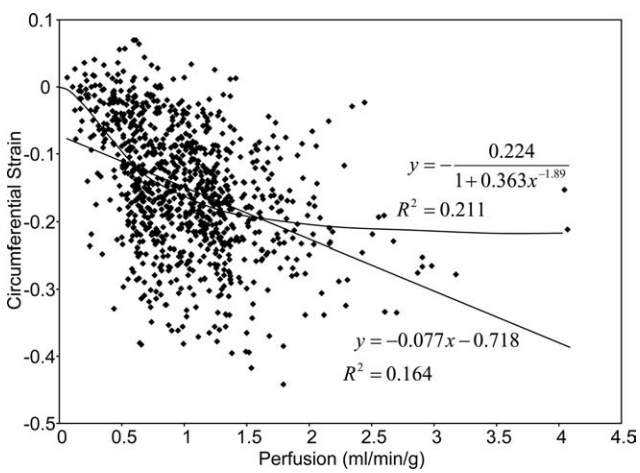

FIG. 9. Correlation of circumferential strain versus perfusion in STEMI patients. Sigmoidal Hill curve fitting gives higher correlation coefficient than linear regression (black line).

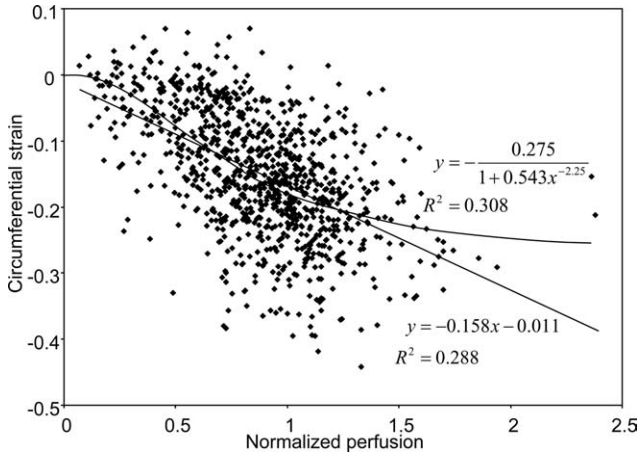

FIG. 10. Correlation of circumferential strain versus normalized perfusion in STEMI patients. The sigmoidal Hill curve fits the data better than linear function.

measure myocardial perfusion and strain simultaneously. The absolute perfusion measurements matched well with the reference standard microsphere measurements in light of prior validation studies of saturation recovery sequences. For example, in one of the first swine hyperemia studies using a saturation recovery turbo fast low angle shot (TurboFLASH) sequence (11) the correlation between MRI relative perfusion index and microsphere absolute perfusion was $R^2 = 0.77$ over the flow range of 0 to 4.1 mL/min/g. A later canine study using a multislice saturation recovery segmented echo-planar imaging sequence achieved $R^2 = 0.50$ to 0.76 for resting flow (12). In a more recent canine hyperemia study using a double-injection technique and a saturation recovery sequence to quantify absolute flow (40), a high correlation of $R^2 = 0.88$ was achieved between MR and microsphere measures over the flow range of 0 to 5.0 mL/min/g. The flow range of the present study is 0 to 1.2 mL/min/g. Since, given the same measurement error, the correlation tends to be tighter with wider ranges of flow, the displacement-encoded sequence was able to yield comparable to better accuracy relative to the saturation recovery sequences.

While contraction in the through-slice direction will slightly reduce the DENSE signal level (7,41), it does not affect the perfusion measurement. This is because perfusion estimation is based on the relative change of signal level pre- and postcontrast injection. Tissue deformation and other non-contrast-related factors are constant throughout the scan and thus do not affect the perfusion estimation.

In the patient study, the performance of this approach was primarily determined by errors in image registration, which accounted for 87.5% of the failed slices. Elastic image registration is affected by dynamic image intensity changes during contrast first-pass, as well as through-slice motion. This step is therefore the focus of further improvement of this methodology.

The relationship between myocardial perfusion and function has been extensively investigated (39,42–47). In earlier studies, perfusion was usually measured by microspheres, while the wall thickening/shortening was quantified with sonomicrometry (39,42–45) or tagged MRI (46). Spatial matching between the two measurements was a persistent technical challenge. It has been stated that (48) "no combination of techniques to measure regional myocardial blood flow and function has the spatial and temporal resolution to quantify the history and thus pathogenesis of a given observed contractile dysfunction and unequivocally either prove or disprove the role of perfusion-contraction matching in the time course of its development." The current pulse sequence potentially provides a means to resolve this problem.

In our small group of STEMI patients, the correlation between circumferential strain and absolute perfusion at rest was found to be marginal and was strengthened by normalizing regional perfusion to the mean of the remote normoperfused area. Previous studies in animal models came to the same conclusion (39,43,46,48). This lack of tight correlation is also seen in our pig study. It confirms what previous studies have found (39,42–48) and attributed to a degree of physiologic decoupling between perfusion and mechanical function at the basal rest condition. Additionally, the current study focused on myocardial circumferential strain for two reasons. One is that it is closely associated with the active shortening of the muscle fibers and linearly related to ejection fraction (49). The second is that the radial strain contains higher errors from edge effects at the endo- and epicardial surfaces (28).

The parameter of short-term contrast washout rate is the product of perfusion and contrast extraction across the capillary wall (50,51). In the patient group, the high level of correlation between this parameter and absolute perfusion implies that the contrast extraction in the myocardial tissue was relatively unchanged by the pathologic condition in these patients (51).

The current methodology has limitations. Only two of the three DENSE slices provided end-systolic strain. This may be remedied with a modified ECG trigger scheme where displacement encoding occurs in end systole and image acquisition occurs in late diastole. The tradeoff is that automatic determination of systole duration according to established formulas may be inaccurate in some patients. The single-shot data acquisition also limited the strain measurement to a single cardiac phase, and the myocardial slices have different cardiac phases due to the different trigger delay times.

The AIF-based estimation of perfusion makes several assumptions. First is that T_2* effects on the AIF blood pool signal were negligible, given the 1.2-ms echo time of the fast gradient-recalled-echo readout. To verify this point, we imaged Gd-DTPA solution phantoms of concentrations up to 10 mM, which is higher than the peak of the injection bolus (~5 mM). The linearity between $\ln(1 - I/I_0)$ and [Gd-DTPA] held up well for all concentrations (Fig. 11), showing that the T_2* effect in the blood pool was negligible.

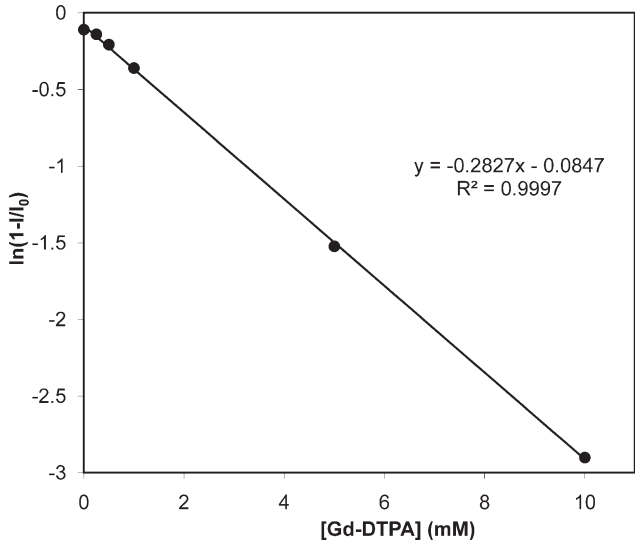

FIG. 11. Verification of the saturation recovery relationship between the AIF image intensity and [Gd-DTPA] in solution phantoms of various concentrations. All sequence parameters were the same as in the human study.

The second assumption is that the tFISP DENSE image myocardial signal follows a simple T_1 relaxation of $I = I_0 e^{-R_1 \cdot Tm}$, and that the relaxation rate is $R_1 = R_{10}$ + (Gd-DTPA relaxivity) × [Gd-DTPA], where the same Gd-DTPA relaxivity value governs both this relationship and the AIF image intensities, such that we can quantify absolute perfusion using the AIF-based deconvolution described in Appendix A. This assumption was also validated in phantoms. Several aspects of this assumption are addressed below.

The first is whether the DENSE tFISP image intensity follows a simple exponential decay of $I = I_0 \exp(-a \times [\text{Gd-DTPA}])$ relative to contrast concentration, given the complex T_1 and T_2 dependence of tFISP signal in a transient phase. Scheffler (52) derived image intensity of a standard tFISP sequence in a transient phase and showed that it approaches the steady state following an exponential relationship. This was verified experimentally by Wang and coauthors (53) in first-pass myocardial diffusion imaging. However, these results cannot be directly applied to our experiment for two reasons. The first and basic reason is that the modified tFISP readout in the DENSE image only acquires displacement-encoded magnetization that is not replenished by T_1 relaxation (6,28,29). This spin dynamics differs substantially from the previous two studies. The second difference between the current pulse sequence and the previous studies is that we employed a ramped flip angle scheme to equalize the echo amplitudes in the readout train, which likely further complicates the T_1 and T_2 dependence of the image intensity. For these reasons, we determined experimentally the relationship between tFISP DENSE image intensity and [Gd-DTPA] in several agarose gel phantoms doped with Gd-DTPA, up to 1.0-mM concentration. This is beyond the peak myocardial concentration (54). Figure 12 shows the linear relationship between $\ln(I/I_0)$ and [Gd-DTPA], with $R^2 = 0.990$. Therefore, despite the complexity of T_1 and T_2 dependence associated with the tFISP readout, the DENSE signal follows a simple exponential decay relative to [Gd-DTPA] in the range of 0- to 1.0-mM concentration.

The second question is whether the apparent decay rate of the tFISP DENSE image intensity is the true R_1, or, in terms that are relevant to the perfusion estimation, whether the apparent relaxivity of Gd-DTPA derived from the exponential relationship is the true relaxivity. The slope in Fig. 12 yields an apparent relaxivity of 5.55 mM^{-1} sec^{-1}. Tofts and coauthors (55) measured a relaxivity of 4.5 mM^{-1} sec^{-1} in agarose gel. Therefore, the tFISP images likely overestimate the relaxivity of Gd-DTPA. However, the AIF-based perfusion estimates are valid as long as this apparent relaxivity is the same as the one in the AIF signal.

Therefore, the third and most relevant question is whether the apparent Gd-DTPA relaxivity is the same in the AIF images and the tFISP images. The relationship between the AIF image intensity and [Gd-DTPA] was investigated in several solution phantoms, ranging from 0- to 10-mM concentration. As described in the "Materials and Methods" section, the AIF image is a saturation recovery image using a TurboFLASH readout. In the phantom study, the AIF intensity follows the saturation recovery relationship of $\ln(1 - I/I_0) = a + b \times [\text{Gd-DTPA}]$ with high fidelity (Fig. 11). Using the nominal saturation-recovery time of 50 ms, which is the interval between spin saturation and the time of the central *k*-space echo, the Gd-DTPA relaxivity was calculated to be 5.65 mM^{-1} sec^{-1}. This value was 2% above the one from the tFISP DENSE images, which would lead to a 2% error in perfusion values. However, by setting the AIF relaxivity equal to the tFISP DENSE image relaxivity, we obtain a calibrated AIF saturation-recovery time of 50.9 ms. This calibrated time can then be used to obtain the correct perfusion levels.

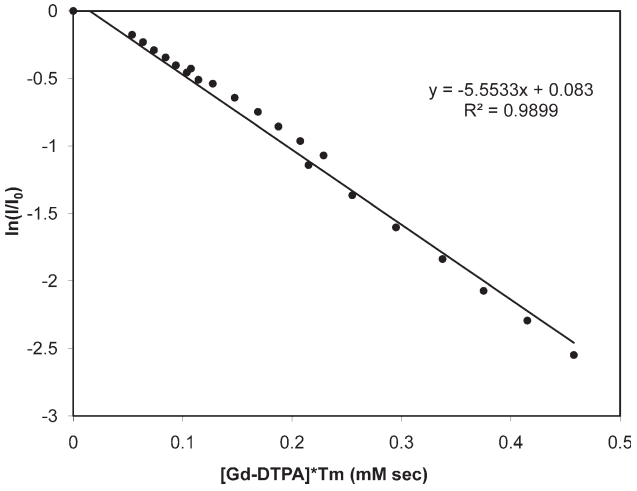

FIG. 12. Dependence of the normalized DENSE image intensity on [Gd-DTPA] in several doped agarose gel phantoms. All sequence parameters, including Tm times, were the same as in the human study. It shows that the image intensity follows simple exponential decay relative to contrast concentration.

Last, dynamic changes of the myocardial resonance frequency during the first pass may affect the tFISP image intensity. Ferreira and coauthors (56) measured myocardial frequency shifts during the first pass of Gd-DTPA at the same dose of 0.1 mmol/kg as this study and a higher injection rate. They found that the shifts were within the range of [−69, 85] Hz, and maximal shifts occurred in horizontal hearts. They proposed that in the worst-case scenario, the maximal shift from Gd-DTPA may combine with the inherent offset from the posterior cardiac vein to reach a level that can cause significant signal loss in tFISP images of 2.5 ms pulse repetition time. This is a limitation of tFISP-based perfusion imaging.

The temporal resolution of image acquisition is limited by the time needed for magnetization recovery. At high flow rates, the temporal resolution may need to be substantially higher than the short-term contrast washout rate in order to accurately measure the amplitude of the myocardial intensity drop. Therefore, measuring hyperemic flow is a potential limitation of this pulse sequence and will need to be tested experimentally.

In the pig study, some had heart rates at or above 100 beats per minute, and it became necessary to waited 2 heart beats between acquisitions to allow magnetization recovery. In the post-angioplasty STEMI patients the heart rates were all below 80 beats per minute and some were on β-blocker medication, so two R-to-R intervals were used for ECG triggers. In general, a better strategy may be to set a low threshold of the interval between acquisitions in the pulse sequence, such that it automatically adjusts the number of heartbeats between acquisitions according to heart rates.

The current study protocol did not permit stress testing, which potentially yields tighter correlation between flow and function (57). The main constraint in applying this sequence to stress imaging is the high heart rate and short systole and diastole periods. At heart rates of 150 beats per minute or higher, only one of the three DENSE slices will have the correct delay time to provide end-systolic strain. A solution around this limitation may be a rotating order of the trigger delays of the slices, in which each slice will be acquired first in turn, and corresponding adaptation of the image processing methods.

In summary, this study shows that a displacement-encoded pulse sequence is able to quantify both myocardial perfusion and strain distributions in a single scan.

APPENDIX A

Flow Estimation by Fermi Model-Base Deconvolution

To estimate the absolute perfusion level from the dynamic changes of the DENSE image intensities during the passage of the bolus of contrast agent, we followed the constrained deconvolution method using a Fermi function model described by Jerosch-Herold et al. (15) and Axel (58). Denote the time of the starting of the bolus infusion as $t = 0$; then the Fermi function model relates the myocardial concentration of contrast agent at time t and location (x, y), $c_m(x, y, t)$ to the arterial blood concentration of contrast agent, $c_a(t)$, through the convolution formula

$$c_m(x,y,t) = F(x,y)\int_0^t c_a(\tau)\frac{1}{\exp\{k(x,y)[\tau-\tau_d(x,y)]\}+1}\,d\tau, \quad [A1]$$

where the value F is the myocardial perfusion rate, the value τ_d accounts for the time delay between the arterial concentration curve $c_a(t)$ in the aorta and the input at the region of interest in the myocardium, and the value k is the contrast washout rate. To proceed further, we need to know the myocardial concentration $c_m(x, y, t)$ for each pixel, as well as the AIF $c_a(t)$.

The AIF was measured from the aortic blood pool signal in the saturation-recovery AIF slice, which was imaged immediately following the displacement-encoding block (Fig. 2). It was acquired without refocusing the displacement-encoding gradients, and thus the displacement-encoding block acted as the saturation prep. The AIF image intensity was

$$I_a(t) = I_0\{1-\exp[-T_s\cdot(R_{1b}+\alpha\cdot c_a(t))]\}, \quad [A2]$$

where I_0 is the image intensity in the absence of the displacement-encoding block, T_s is the effective saturation recovery time, R_{1b} is the native T_1 relaxation rate of blood of 0.67 $\sec^{-1}$ at 1.5 T (59), and α is the efficiency of T_1 relaxation of the contrast agent. I_0 was measured with a separate acquisition without the displacement-encoding block at the end of the scan. The effective saturation recovery time T_s was specific to the fast gradient-recalled-echo acquisition of the AIF slice and was obtained through a calibration process using several phantoms of known T_1s:

$$I_n = I_{n0}\{1-\exp[-T_s/T_{1n}]\}, \quad [A3]$$

where I_n and I_{n0} were the AIF image and proton density image intensities of the nth phantom, and T_{1n} was the T_1 of the nth phantom. The saturation recovery time T_s was obtained through linear regression in the $\log(1 - I_n/I_{n0})$ versus $1/T_{1n}$ plot. Once the saturation recovery time was known, the AIF was then derived from Eq. A2 to within the unknown efficiency coefficient α

$$\alpha\cdot c_a(t) = -\frac{\ln[1-I_a(t)/I_0]}{T_s} - R_{1b}. \quad [A4]$$

We next look at the myocardial contrast concentration $c_m(x, y, t)$ and its effect on the DENSE slices. The three DENSE slices were acquired with single-shot true-FISP readout of sequential k-space coverage. Each slice took 100 ms to acquire. The time delays between the displacement-encoding block and the centers of the slice acquisitions were therefore

$$T_{mj} = (200+100\cdot j)(ms),\ j=0,1,2. \quad [A5]$$

The DENSE image signal intensity is influenced by T_1 decay during the time delay in the form

$$I_j(x,y,t) = I_{j0}\exp\{-T_{mj}\cdot[R_{1m}+\alpha\cdot c_{mj}(x,y,t)]\},\ j=0,1,2, \quad [A6]$$

where R_{1m} is the native T_1 relaxation rate of the myocardium, and we assume complete magnetization recovery.

Our image acquisition began at 30 sec before bolus infusion. During the precontrast period

$$I_j(x,y,t<0) = I_{j0}\exp(-T_{mj}\cdot R_{1m}),\ j=0,1,2. \qquad [A7]$$

The time average of the images during this period provided the reference images

$$I_{rj}(x,y) = <I_j(x,y,t<0)>_t,\ j=0,1,2. \qquad [A8]$$

Combining Eqs. A6 and A8 yielded the myocardial contrast concentration to within the efficiency coefficient α

$$\alpha\cdot c_{mj}(x,y,t) = -\ln[I_j(x,y,t)/I_{rj}(x,y)]/T_{mj},\ j=0,1,2. \qquad [A9]$$

By using this equation, the relative signal intensity change instead of the absolute signal intensity is used for perfusion estimation, so other factors that affect the image signal intensity, such as coil profile, will be removed, with no need for additional correction. We then assume that the relaxation efficiency α of the contrast agent is the same in the arterial blood pool as in the myocardium. The AIF from Eq. A4 and the myocardial contrast from Eq. A9 were then input into Fermi function model of Eq. A1. Through the Marquardt-Levenberg nonlinear least squares fitting algorithm (Interactive Data Language; ITT, White Plains, NY), the perfusion $F(x,y)$ and washout rate $k(x,y)$ were estimated for each pixel. If the fitting algorithm failed to converge for a specific pixel, then that pixel was left blank in the resulting perfusion maps and was excluded in the statistical analyses.

APPENDIX B

Simulation Study on the Effect of Noise and Sampling Rate on Perfusion Estimation

The same Fermi function convolution model of Appendix A was used to simulate myocardial contrast concentration from a known AIF. The AIF is taken from one of the pig experiments after being fitting to γ-variate function (15):

$$c(t) = C\cdot t^{v}\cdot\exp(-t/u). \qquad [B1]$$

A series of myocardial signal time-intensity traces was generated according to Eq. A1, with perfusion levels F_{real} ranging between 0.25 and 2.5 mL/min/g, and corresponding washout rates k according to the linear relationship between the two. Normally distributed random noise of standard deviation (σ_N) of 10%, 15%, and 20% of the precontrast signal intensity was added to the time-intensity traces. The resulting noisy signal, as well as the AIF, was sampled at the rate of once per 2 sec. These were the simulated myocardial image signal. They were input into the flow estimation routine to produce a simulated measurement of perfusion F_{est}. For each noise level and perfusion level, 1000 simulations were performed. The root-mean-squared error of the estimated flow RMS(F_{est}) and the normalized error RMS(F_{est})/F_{real} were plotted in Fig. B1.

The results show that for the noise level of 15%, the relative uncertainty in perfusion measurement is below 30% when the perfusion level is greater than 0.75 mL/min/g, and the uncertainty stays below 0.2 mL/min/g for lower perfusion levels. This was regarded as acceptable in the patient study.

In the patient data, the noise level of each pixel was measured by the error of the curve fitting, which is defined as the RMS difference between the actual signal and the fitted values. The simulations showed that the above procedure accurately estimated the true noise levels in the simulated time-intensity curves. In the experimental studies, myocardial pixels with noise levels above 15% were excluded from further processing and left blank in the perfusion maps.

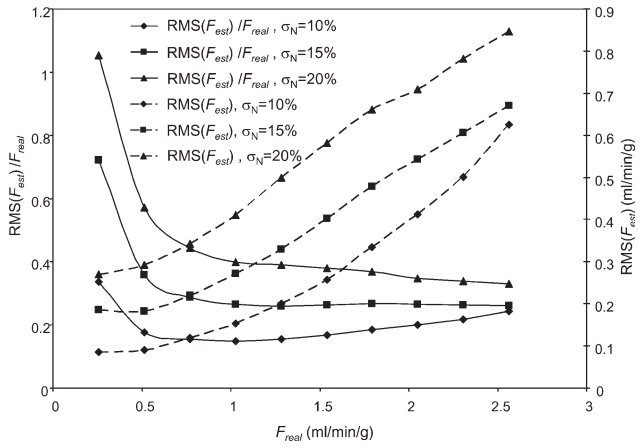

FIG. B1. Absolute and normalized error of flow estimation versus real flow for different levels of noise in the image intensity. The dashed lines represent the root-mean-squared error of flow estimation RMS(F_{est}), and the solid lines represent the normalized error RMS(F_{est})/F_{real}.

REFERENCES

1. Chen Q, Mai VM, Bankier AA, Napadow VJ, Gilbert RJ, Edelman RR. Ultrafast MR grid-tagging sequence for assessment of local mechanical properties of the lungs. Magn Reson Med 2001;45:24–28.
2. Zerhouni EA, Parish DM, Rogers WJ, Yang A, Shapiro EP. Human heart: tagging with MR imaging—a method for noninvasive assessment of myocardial motion. Radiology 1988;169:59–63.
3. Fischer SE, McKinnon GC, Maier SE, Boesiger P. Improved myocardial tagging contrast. Magn Reson Med 1993;30:191–200.
4. Reichek N. MRI myocardial tagging. J Magn Reson Imaging 1999;10: 609–616.
5. Streif JU, Herold V, Szimtenings M, Lanz TE, Nahrendorf M, Wiesmann F, Rommel E, Haase A. In vivo time-resolved quantitative motion mapping of the murine myocardium with phase contrast MRI. Magn Reson Med 2003;49:315–321.
6. Bennett EE, Pai VM, Wen H. Ultrafast DENSE technique for mapping the volumetric 3D wall motion of the left ventricle. In: ISMRM 10th Annual Scientific Meeting and Exhibition. Honolulu, HI, 2002. p 775.
7. Aletras AH, Ding S, Balaban RS, Wen H. DENSE: displacement encoding with stimulated echoes in cardiac functional MRI. J Magn Reson 1999;137:247–252.
8. Aletras AH, Balaban RS, Wen H. High-resolution strain analysis of the human heart with fast-DENSE. J Magn Reson 1999;140:41–57.
9. Kellman P, Aletras AH, Hsu LY, McVeigh ER, Arai AE. T2* measurement during first-pass contrast-enhanced cardiac perfusion imaging. Magn Reson Med 2006;56:1132–1134.
10. Hsu LY, Rhoads KL, Holly JE, Kellman P, Aletras AH, Arai AE. Quantitative myocardial perfusion analysis with a dual-bolus

contrast-enhanced first-pass MRI technique in humans. J Magn Reson Imaging 2006;23:315–322.
11. Wilke N, Jerosch-Herold M, Wang Y, Huang Y, Christensen BV, Stillman AE, Ugurbil K, McDonald K, Wilson RF. Myocardial perfusion reserve: assessment with multisection, quantitative, first-pass MR imaging. Radiology 1997;204:373–384.
12. Epstein FH, London JF, Peters DC, Goncalves LM, Agyeman K, Taylor J, Balaban RS, Arai AE. Multislice first-pass cardiac perfusion MRI: validation in a model of myocardial infarction. Magn Reson Med 2002;47:482–491.
13. Kellman P, Derbyshire JA, Agyeman KO, McVeigh ER, Arai AE. Extended coverage first-pass perfusion imaging using slice-interleaved TSENSE. Magn Reson Med 2004;51:200–204.
14. Jerosch-Herold M, Swingen C, Seethamraju RT. Myocardial blood flow quantification with MRI by model-independent deconvolution. Med Phys 2002;29:886–897.
15. Jerosch-Herold M, Wilke N, Stillman AE. Magnetic resonance quantification of the myocardial perfusion reserve with a Fermi function model for constrained deconvolution. Med Phys 1998;25:73–84.
16. McNamara MT, Tscholakoff D, Revel D, Soulen R, Schechtmann N, Botvinick E, Higgins CB. Differentiation of reversible and irreversible myocardial injury by MR imaging with and without gadolinium-DTPA. Radiology 1986;158:765–769.
17. Peshock RM, Malloy CR, Buja LM, Nunnally RL, Parkey RW, Willerson JT. Magnetic resonance imaging of acute myocardial infarction: gadolinium diethylenetriamine pentaacetic acid as a marker of reperfusion. Circulation 1986;74:1434–1440.
18. Kim RJ, Fieno DS, Parrish TB, Harris K, Chen EL, Simonetti O, Bundy J, Finn JP, Klocke FJ, Judd RM. Relationship of MRI delayed contrast enhancement to irreversible injury, infarct age, and contractile function. Circulation 1999;100:1992–2002.
19. Judd RM, Kim RJ. Imaging time after Gd-DTPA injection is critical in using delayed enhancement to determine infarct size accurately with magnetic resonance imaging. Circulation 2002;106:e6; author reply e6.
20. Judd RM, Wagner A, Rehwald WG, Albert T, Kim RJ. Technology insight: assessment of myocardial viability by delayed-enhancement magnetic resonance imaging. Nat Clin Pract Cardiovasc Med 2005;2:150–158.
21. Kim RJ, Chen EL, Lima JA, Judd RM. Myocardial Gd-DTPA kinetics determine MRI contrast enhancement and reflect the extent and severity of myocardial injury after acute reperfused infarction. Circulation 1996;94:3318–3326.
22. Gilson WD, Yang Z, French BA, Epstein FH. Complementary displacement-encoded MRI for contrast-enhanced infarct detection and quantification of myocardial function in mice. Magn Reson Med 2004;51:744–752.
23. el Ibrahim SH, Stuber M, Kraitchman DL, Weiss RG, Osman NF. Combined functional and viability cardiac MR imaging in a single breathhold. Magn Reson Med 2007;58:843–849.
24. Le Y, Kellman P, Taylor J, Bennett E, Lucas K, Chefd'Hotel C, Lorenz CH, Croisille P, Wen H. Simultaneous myocardial perfusion and strain imaging with displacement-encoded MRI. Chicago, IL, 2008. p 382.
25. Le Y, Kellman P, Taylor J, Bennett E, Lucas K, Chefd'Hotel C, Lorenz CH, Wen H. Simultaneous myocardial first-pass perfusion and strain imaging with DENSE. J Card Magn Reson 2008;10(suppl 1):95–96.
26. Rouviere O, Reynolds C, Hulshizer T, Rossman P, Le Y, Felmlee JP, Ehman RL. MR histological correlation: a method for cutting specimens along the imaging plane in animal or ex vivo experiments. J Magn Reson Imaging 2006;23:60–69.
27. Cerqueira MD, Weissman NJ, Dilsizian V, Jacobs AK, Kaul S, Laskey WK, Pennell DJ, Rumberger JA, Ryan T, Verani MS. Standardized myocardial segmentation and nomenclature for tomographic imaging of the heart: a statement for healthcare professionals from the Cardiac Imaging Committee of the Council on Clinical Cardiology of the American Heart Association. Circulation 2002;105:539–542.
28. Wen H, Marsolo KA, Bennett EE, Kutten KS, Lewis RP, Lipps DB, Epstein ND, Plehn JF, Croisille P. Adaptive postprocessing techniques for myocardial tissue tracking with displacement-encoded MR imaging. Radiology 2008;246:229–240.
29. Kim D, Kellman P. Improved cine displacement-encoded MRI using balanced steady-state free precession and time-adaptive sensitivity encoding parallel imaging at 3 T. NMR Biomed 2007;20:591–601.
30. Zhong X, Spottiswoode BS, Cowart EA, Gilson WD, Epstein FH. Selective suppression of artifact-generating echoes in cine DENSE using through-plane dephasing. Magn Reson Med 2006;56:1126–1131.
31. Hermosillo G, Chefd'Hotel C, Faugeras O. Variational methods for multimodal image matching. Int J Comput Vision 2002;50:329–343.
32. Kellman P, Chefd'hotel C, Lorenz CH, Mancini C, Arai AE, McVeigh ER. Fully automatic, retrospective enhancement of real-time acquired cardiac cine MR images using image-based navigators and respiratory motion-corrected averaging. Magn Reson Med 2008;59:771–778.
33. Le Y, Kellman P, Bennett EE, Lin A, Chefd'Hotel C, Lorenz CH, Wen H. Free-breathing single-shot DENSE myocardial strain imaging using deformable registration. J Card Magn Reson 2008;10(suppl 1):A207.
34. Bernstein MA, Grgic M, Brosnan TJ, Pelc NJ. Reconstructions of phase contrast, phased array multicoil data. Magn Reson Med 1994;32:330–334.
35. Gatehouse PD, Elkington AG, Ablitt NA, Yang GZ, Pennell DJ, Firmin DN. Accurate assessment of the arterial input function during high-dose myocardial perfusion cardiovascular magnetic resonance. J Magn Reson Imaging 2004;20:39–45.
36. Kim D, Axel L. Multislice, dual-imaging sequence for increasing the dynamic range of the contrast-enhanced blood signal and CNR of myocardial enhancement at 3T. J Magn Reson Imaging 2006;23:81–86.
37. Kim D, Gilson WD, Kramer CM, Epstein FH. Myocardial tissue tracking with two-dimensional cine displacement-encoded MR imaging: development and initial evaluation. Radiology 2004;230:862–871.
38. Feng L, Donnino R, Babb J, Axel L, Kim D. Numerical and in vivo validation of fast cine displacement-encoded with stimulated echoes (DENSE) MRI for quantification of regional cardiac function. Magn Reson Med 2009;62:682–690.
39. Weintraub WS, Hattori S, Agarwal JB, Bodenheimer MM, Banka VS, Helfant RH. The relationship between myocardial blood flow and contraction by myocardial layer in the canine left ventricle during ischemia. Circ Res 1981;48:430–438.
40. Christian TF, Rettmann DW, Aletras AH, Liao SL, Taylor JL, Balaban RS, Arai AE. Absolute myocardial perfusion in canines measured by using dual-bolus first-pass MR imaging. Radiology 2004;232:677–684.
41. Fischer SE, Stuber M, Scheidegger MB, Boesiger P. Limitations of stimulated echo acquisition mode (STEAM) techniques in cardiac applications. Magn Reson Med 1995;34:80–91.
42. Gallagher KP, Matsuzaki M, Osakada G, Kemper WS, Ross J Jr. Effect of exercise on the relationship between myocardial blood flow and systolic wall thickening in dogs with acute coronary stenosis. Circ Res 1983;52:716–729.
43. Gallagher KP, Matsuzaki M, Koziol JA, Kemper WS, Ross J Jr. Regional myocardial perfusion and wall thickening during ischemia in conscious dogs. Am J Physiol 1984;247(5 pt 2):H727–738.
44. Vatner SF. Correlation between acute reductions in myocardial blood flow and function in conscious dogs. Circ Res 1980;47:201–207.
45. Stowe DF, Mathey DG, Moores WY, Glantz SA, Townsend RM, Kabra P, Chatterjee K, Parmley WW, Tyberg JV. Segment stroke work and metabolism depend on coronary blood flow in the pig. Am J Physiol 1978;234:H597–607.
46. Moore CC, McVeigh ER, Zerhouni EA. Noninvasive measurement of three-dimensional myocardial deformation with tagged magnetic resonance imaging during graded local ischemia. J Cardiovasc Magn Reson 1999;1:207–222.
47. Ross J Jr. Myocardial perfusion-contraction matching: implications for coronary heart disease and hibernation. Circulation 1991;83:1076–1083.
48. Heusch G, Schulz R. Perfusion-contraction match and mismatch. Basic Res Cardiol 2001;96:1–10.
49. Weidemann F, Jamal F, Kowalski M, Kukulski T, D'Hooge J, Bijnens B, Hatle L, De Scheerder I, Sutherland GR. Can strain rate and strain quantify changes in regional systolic function during dobutamine infusion, B-blockade, and atrial pacing? Implications for quantitative stress echocardiography. J Am Soc Echocardiogr 2002;15:416–424.
50. Larsson HB, Stubgaard M, Sondergaard L, Henriksen O. In vivo quantification of the unidirectional influx constant for Gd-DTPA diffusion across the myocardial capillaries with MR imaging. J Magn Reson Imaging 1994;4:433–440.
51. Cullen JH, Horsfield MA, Reek CR, Cherryman GR, Barnett DB, Samani NJ. A myocardial perfusion reserve index in humans using first-pass contrast-enhanced magnetic resonance imaging. J Am Coll Cardiol 1999;33:1386–1394.

52. Scheffler K. On the transient phase of balanced SSFP sequences. Magn Reson Med 2003;49:781–783.
53. Wang Y, Moin K, Akinboboye O, Reichek N. Myocardial first pass perfusion: steady-state free precession versus spoiled gradient echo and segmented echo planar imaging. Magn Reson Med 2005;54:1123–1129.
54. Cernicanu A, Axel L. Theory-based signal calibration with single-point T1 measurements for first-pass quantitative perfusion MRI studies. Acad Radiol 2006;13:686–693.
55. Tofts PS, Shuter B, Pope JM. Ni-DTPA doped agarose gel—a phantom material for Gd-DTPA enhancement measurements. Magn Reson Imaging 1993;11:125–133.
56. Ferreira P, Gatehouse P, Bucciarelli-Ducci C, Wage R, Firmin D. Measurement of myocardial frequency offsets during first pass of a gadolinium-based contrast agent in perfusion studies. Magn Reson Med 2008;60:860–870.
57. Nagel E, Lorenz C, Baer F, Hundley WG, Wilke N, Neubauer S, Sechtem U, van der Wall E, Pettigrew R, de Roos A, Fleck E, van Rossum A, Pennell DJ, Wickline S. Stress cardiovascular magnetic resonance: consensus panel report. J Cardiovasc Magn Reson 2001;3:267–281.
58. Axel L. Tissue mean transit time from dynamic computed tomography by a simple deconvolution technique. Invest Radiol 1983;18: 94–99.
59. Duewell SH, Ceckler TL, Ong K, Wen H, Jaffer FA, Chesnick SA, Balaban RS. Musculoskeletal MR imaging at 4 T and at 1.5 T: comparison of relaxation times and image contrast. Radiology 1995;196: 551–555.